NUMERICAL SIMULATIONS FOR THE ARZ MODEL FOR VEHICULAR TRAFFIC WITH GENERAL POINT CONSTRAINTS ON THE DENSITY FLUX

Carlotta Donadello, Bastien Polizzi, Ulrich Razafison, Julien Yves Rolland, Massimiliano D. Rosini

NUMERICAL SIMULATIONS FOR THE ARZ MODEL FOR VEHICULAR TRAFFIC WITH GENERAL POINT CONSTRAINTS ON THE DENSITY FLUX

C. DONADELLO, B. POLIZZI, U. RAZAFISON, J.Y. ROLLAND, AND M.D. ROSINI

ABSTRACT. In this paper we investigate numerically the model for vehicular traffic proposed in [B. Andreianov, C. Donadello, M.D. Rosini, A second order model for vehicular traffics with local point constraints on the flow, Mathematical Models and Methods in Applied Sciences 26 (4) (2016) 751-802]. The model is obtained by coupling the ARZ system with point constraints on the density flux, and reproduces traffic behavior at bottlenecks. We implement an adapted version of the Glimm scheme featuring a non-classical Riemann solver at the constraint locations. We show its numerical convergence and its ability to correctly capture the evolution of both conservative and Riemann invariant variables in all situations, including those involving the vacuum.

Our scheme allows to conduct a number of numerical experiments to prove that the model reproduces several typical phenomena such as capacity drop, faster is slower effect and phantom jams. Beyond the theoretical results obtained in the aforementioned paper, we also consider point constraints whose values are determined by a Lipschitz continuous function of time, or depend non-locally on the solution itself.

1. INTRODUCTION

The macroscopic model developed by Andreianov, Donadello and Rosini in [4] describes the evolution of vehicular traffic along a road when the maximal flow capacity is reduced point-wise due to the presence of obstacles, such as toll booths, traffic lights, or construction sites. We refer to it as the ADR model.

The ADR model consists of the classical second order Aw-Rascle-Zhang (ARZ) model [7, 37], supplemented by local point constraint inequalities on the density flux, enforced at a finite number of constraint locations. The conserved variables of the system are ρ and y, the (mean) density and the generalized momentum of vehicles, respectively. However, expressing the equations in terms of the Riemann invariant coordinates, namely the velocity v and the Lagrangian marker w, simplifies the mathematical analysis, see Section A for more details.

In the case of a single constraint located at $x = 0$, the ADR model writes as a constrained Cauchy problem for a 2×2 hyperbolic system of conservation laws in one space dimension as follows

$$\begin{cases} \rho(v,w)_t + [v\,\rho(v,w)]_x = 0, & (t,x) \in \mathbb{R}_+ \times \mathbb{R}, \\ y(v,w)_t + [v\,y(v,w)]_x = 0, & (t,x) \in \mathbb{R}_+ \times \mathbb{R}, \\ (v,w)(0,x) = (\bar{v},\bar{w})(x), & x \in \mathbb{R}, \\ [v\,\rho(v,w)](t,0^{\pm}) \leqslant Q(t), & t \in \mathbb{R}_+. \end{cases} \tag{1}$$

Here $(\bar{v},\bar{w}) \in \mathcal{W} = \{(v,w) \in \overline{\mathbb{R}}_+^2 : v \leqslant w\}$ represents the initial datum,

$$(v,w)\colon \overline{\mathbb{R}}_+ \times \mathbb{R} \to \mathcal{W},$$

2010 *Mathematics Subject Classification.* 35L65, 90B20, 65M12, 76M12.

Key words and phrases. Glimm scheme, system of conservation laws, point constraint, vehicular traffic, ARZ model, ADR model, capacity drop, faster is slower, phantom jams, Braess' paradox.

is the dependent variable, and we recover the conservative variables $\rho, y \colon \mathcal{W} \to \overline{\mathbb{R}}_+$ by

$$\rho(v,w) = p^{-1}(w-v), \qquad y(v,w) = w\,p^{-1}(w-v). \tag{2}$$

The function p in the equations above, called pressure or velocity offset in the literature, represents the ability of drivers to anticipate the behavior of the neighboring traffic and satisfies the following conditions:

$$\begin{aligned} &p(0) = 0, \qquad \lim_{\rho\downarrow 0}\left[\rho^2 p'(\rho)\right] = 0, \qquad \lim_{\rho\downarrow 0}\left[\frac{\rho\,p''(\rho)}{p'(\rho)}\right] < +\infty, \\ &p'(\rho) > 0 \qquad \text{and} \qquad p'(\rho) + \rho\,p''(\rho) > 0 \qquad \text{for all } \rho > 0. \end{aligned} \tag{3}$$

At last, $Q \colon \overline{\mathbb{R}}_+ \to \overline{\mathbb{R}}_+$ prescribes the maximal density flow allowed through $x = 0$, and $(v,w)(t,0^-)$ denotes the left measure theoretic trace along $x = 0$, implicitly defined by

$$\lim_{\varepsilon\downarrow 0} \frac{1}{\varepsilon} \int_{\mathbb{R}_+} \int_{-\varepsilon}^{0} \left\| (v,w)(t,x) - (v,w)(t,0^-) \right\| \, \phi(t,x) \, \mathrm{d}x \, \mathrm{d}t = 0, \qquad \text{for all } \phi \in C_c^\infty(\mathbb{R}^2;\mathbb{R}).$$

The right measure theoretic trace, $(v,w)(t,0^+)$, is defined analogously.

By (2), the vacuum $\rho = 0$ corresponds to the half line $\mathcal{W}_0 = \{(v,w) \in \mathcal{W} : v = w\}$ and the non-vacuum states $\rho \neq 0$ to $\mathcal{W}_0^c = \mathcal{W} \setminus \mathcal{W}_0$.

The existence result established in [4] for system (1) requires that the function Q is given beforehand and is piece-wise constant in time, see A for more details. However, data analysis, e.g. [24, 22, 28], suggests that the capacity of toll plazas (i.e. the maximum number of vehicles that can flow through them in a given time interval) depends non-locally on the solution. Indeed, it may decrease under high-density conditions that occur upstream of the toll booths, mainly due to vehicles switching or jockeying between queues before reaching the servers. This *capacity drop* phenomenon leads to significant increase of travel time delay and air pollution. Also, as a heavy congestion forms upstream of a toll plaza its efficiency reduces, accidents become more probable due to stop-and-go behaviors, and the *egress time* increases (i.e. the time gap between the passage of the first and the last vehicle through the toll booths). These effects, strongly associated to the ability of drivers to anticipate the evolution of traffic and estimate the queues' length, cannot be captured by only using a given constraint function, piece-wise constant in time.

The theoretical analysis of a more general version of the model, featuring Lipschitz in time and possibly non-local constraint functions Q in the flavor of [2], cannot be conducted via the approach used in [4], which relies on the combination of the wave-front tracking and operator splitting methods, as we miss the stability estimates which guarantee the consistency of the approximation.

The aim of this paper is to provide a number of examples showing that such generalized ADR models qualitatively reproduce the main effects related to capacity drop, namely the so-called Faster-Is-Slower (FIS) effect, see [20] and the references therein, the Braess' paradox and phantom jams, i.e. jams that arise in the absence of any obstacles, see [34] for the results of a related empirical experiment. Notice that we apply the theory of point constraints only as a trigger and not as the essential origin of a traffic phantom jam. Moreover, for real life applications, the function Q, representing the upper bound of the constrained density flux, must be deduced from empirical observations.

In the first part of the paper, we introduce an adapted version of the Glimm scheme, which features a non-classical Riemann solver at the constraint location, and show its numerical convergence. In Section 2, we introduce the Riemann solvers required for the ADR model and the Glimm scheme. In Section 3, we explain why the Glimm scheme is the most suitable choice for our problem and describe its implementation. Subsequently, we show its numerical convergence. Initially, we assume that the value of Q is given and piecewise constant in time, as in [4] (cf. Section 4.1). Next, in Section 4.2, we demonstrate that if the Lagrangian marker w

is constant, the solution computed via our scheme coincides with that of the first order model with a point constraint proposed in [3], computed using the (theoretically and numerically convergent) finite volume scheme studied in [2]. This holds even if the constraint function is Lipschitz continuous in time or depends non-locally in space on the solution itself. The numerical implementation for the latter case relies on a splitting strategy, as in [1, 2], for the first-order model proposed in [3].

In the second part of the paper, we investigate the qualitative behavior of the model. In Section 5, we demonstrate its ability to reproduce phenomena such as phantom jams (Section 5.1), capacity drop (Section 5.2), the FIS effect (Section 5.2.1), and Braess' paradox (Section 5.3). Our final simulation, in Section 5.4, inspired by a problem involving the load capacity of a bridge, illustrates the possibility of considering constraint functions that depend on more than one component of the solution, and fully exploits the richness of the second-order traffic model.

Conclusions and perspectives are presented in Section 6. Finally, in the appendices, we briefly recall analytical results on the ADR model from [4], and we include a test of numerical convergence similar to the one proposed in Example 4.4, but for a constraint function with jump discontinuities.

2. The Riemann solvers in the ADR model and in the Glimm scheme

In this section, we briefly review the two Riemann solvers that serve as building blocks for the analysis of the ADR model, and discuss the minor modifications required for the implementation of the Glimm scheme. We recall that Riemann solvers provide the physical entropy self-similar solutions to Riemann problems, which are Cauchy problems with piecewise constant initial conditions featuring at most one discontinuity at $x = 0$. Details on the definition and the existence of entropy solutions to general Cauchy problems are provided in A. We first present the Riemann solver $\mathcal{RS}$ proposed in [7] for the ARZ model, followed by the Riemann solver $\mathcal{RS}_Q$ introduced in [4] for the ADR model, which is used at the constraint location to enforce the density flux limitation.

Consider the Riemann problem for the ARZ model

$$\begin{cases} \rho(v,w)_t + [v\,\rho(v,w)]_x = 0, & (t,x) \in \mathbb{R}_+ \times \mathbb{R}, \\ y(v,w)_t + [v\,y(v,w)]_x = 0, & (t,x) \in \mathbb{R}_+ \times \mathbb{R}, \\ (v,w)(0,x) = \begin{cases} (v_\ell, w_\ell), & \text{if } x < 0, \\ (v_r, w_r), & \text{if } x \geqslant 0, \end{cases} & x \in \mathbb{R}. \end{cases} \tag{4}$$

Since the first characteristic family is genuinely nonlinear and the second is linearly degenerate, the solution to (4) consists either of a single elementary wave (shock or rarefaction of the first family, or contact discontinuity of the second family) or of the juxtaposition of two waves, one for each of the families, in the order. Notice that, under hypothesis (3), we can implicitly define a function $\mathfrak{P}$ through the equation

$$\mathfrak{P}\left(p(\rho) + \rho\, p'(\rho)\right) = \rho. \tag{5}$$

Definition 2.1 (Riemann solver $\mathcal{RS}$)**.** *For any $W_\ell = (v_\ell, w_\ell), W_r = (v_r, w_r) \in \mathcal{W}$, we define $\mathcal{RS}[W_\ell, W_r] \in C^0\left(\mathbb{R}_+; \mathbf{L}^1_{\mathrm{loc}}(\mathbb{R}; \mathcal{W})\right)$ as follows:*

(1) For any $W_* \in \mathcal{W}$, $\mathcal{RS}[W_*, W_*] = W_*$.

(2) If $W_r \in \mathcal{W}_0^c$, $w_\ell = w_r$ and $v_\ell > v_r$, then $\mathcal{RS}[W_\ell, W_r]$ consists of a shock discontinuity

$$\mathfrak{S}[W_\ell, W_r](\nu) = \begin{cases} W_\ell, & \text{if } \nu < \sigma(W_\ell, W_r), \\ W_r, & \text{if } \nu \geqslant \sigma(W_\ell, W_r), \end{cases}$$

where the propagation speed is given by the Rankine-Hugoniot condition

$$\sigma(W_\ell, W_r) = \frac{v_r\,\rho(W_r) - v_\ell\,\rho(W_\ell)}{\rho(W_r) - \rho(W_\ell)}.$$

(3) If $W_\ell, W_r \in \mathcal{W}_0^c$, $w_\ell = w_r$ and $v_\ell < v_r$, then $\mathcal{RS}[W_\ell, W_r]$ consists of a rarefaction wave

$$\mathfrak{R}[W_\ell, W_r](\nu) = \begin{cases} W_\ell, & \text{if } \nu < \lambda_1(W_\ell), \\ \left(w - p\left(\mathfrak{P}\left(w - \nu\right)\right), w\right), & \text{if } \lambda_1(W_\ell) \leqslant \nu < \lambda_1(W_r), \\ W_r, & \text{if } \nu \geqslant \lambda_1(W_r), \end{cases}$$

where $\mathfrak{P}$ is defined in (5) and

$$\lambda_1(W) = \begin{cases} v - \rho(W)\, p'\left(\rho(W)\right), & \text{if } W \in \mathcal{W}_0^c, \\ w, & \text{if } W \in \mathcal{W}_0. \end{cases}$$

(4) If $W_\ell, W_r \in \mathcal{W}_0^c$ and $v_\ell = v_r$, then $\mathcal{RS}[W_\ell, W_r]$ consists of a contact discontinuity

$$\mathfrak{C}[W_\ell, W_r](\nu) = \begin{cases} W_\ell, & \text{if } \nu < v, \\ W_r, & \text{if } \nu \geqslant v. \end{cases}$$

(5) If $W_\ell, W_r \in \mathcal{W}_0$ and $W_\ell \neq W_r$ then $\mathcal{RS}[W_\ell, W_r] = W_r$.

(6) If $W_\ell \in \mathcal{W}_0^c$ and $W_r \in \mathcal{W}_0$ then $\mathcal{RS}[W_\ell, W_r]$ takes the form

$$\mathcal{RS}[W_\ell, W_r](\nu) = \begin{cases} \mathfrak{R}\big[W_\ell, (w_\ell, w_\ell)\big], & \text{if } \nu < w_\ell, \\ W_r, & \text{if } \nu \geqslant w_\ell. \end{cases}$$

(7) If $W_\ell \in \mathcal{W}_0$ and $W_r \in \mathcal{W}_0^c$, then

$$\mathcal{RS}[W_\ell, W_r](\nu) = \begin{cases} W_\ell, & \text{if } \nu < v_r, \\ W_r, & \text{if } \nu \geqslant v_r. \end{cases}$$

(8) If $W_\ell, W_r \in \mathcal{W}_0^c$ and $v_r < v_\ell < w_\ell$, then $\mathcal{RS}[W_\ell, W_r]$ is the juxtaposition of $\mathfrak{S}[W_\ell, W_m]$ and $\mathfrak{C}[W_m, W_r]$, where $W_m = (v_r, w_\ell) \in \mathcal{W}_0^c$.

(9) If $W_\ell, W_r \in \mathcal{W}_0^c$ and $v_\ell < v_r < w_\ell$, then $\mathcal{RS}[W_\ell, W_r]$ is the juxtaposition of $\mathfrak{R}[W_\ell, W_m]$ and $\mathfrak{C}[W_m, W_r]$, where $W_m = (v_r, w_\ell) \in \mathcal{W}_0^c$.

(10) If $W_\ell, W_r \in \mathcal{W}_0^c$ and $v_\ell < w_\ell \leqslant v_r < w_r$, then

$$\mathcal{RS}[W_\ell, W_r](\nu) = \begin{cases} \mathfrak{R}[W_\ell, W_m](\nu), & \text{if } \nu < v_r, \\ W_r, & \text{if } \nu \geqslant v_r, \end{cases}$$

where $W_m = (w_\ell, w_\ell) \in \mathcal{W}_0$.

We now introduce the Riemann solver corresponding to the Riemann problem for the ADR model

$$\begin{cases} \rho(v,w)_t + \left[v\,\rho(v,w)\right]_x = 0, & (t,x) \in \mathbb{R}_+ \times \mathbb{R}, \\ y(v,w)_t + \left[v\,y(v,w)\right]_x = 0, & (t,x) \in \mathbb{R}_+ \times \mathbb{R}, \\ (v,w)(0,x) = \begin{cases} (v_\ell, w_\ell), & \text{if } x < 0, \\ (v_r, w_r), & \text{if } x \geqslant 0, \end{cases} & x \in \mathbb{R}, \\ \left[v\,\rho(v,w)\right](t, 0^\pm) \leqslant Q, & t \in \mathbb{R}_+, \end{cases} \tag{6}$$

where $Q \in \mathbb{R}_+$ is the constant maximal density flow allowed through $x = 0$. We first need to introduce $\hat{W}(Q,w) = (\hat{v}(Q,w), \hat{w}(Q,w))$ and $\check{W}(Q,w) = (\check{v}(Q,w), \check{w}(Q,w))$ defined for $(Q,w) \in \mathbb{R}_+ \times \overline{\mathbb{R}}_+$ by

$$\begin{aligned} &\hat{w}(Q,w) = w = \check{w}(Q,w), \\ &\hat{v}(Q,w) = \begin{cases} \min\left\{v \in (0,w) : w = v + p(Q/v)\right\} & \text{if } w \in [\tilde{w}(Q), \infty), \\ w - p\left(\dot{\rho}(w)\right) & \text{if } w \in [0, \tilde{w}(Q)), \end{cases} \\ &\check{v}(Q,w) = \begin{cases} \max\left\{v \in (0,w) : w = v + p(Q/v)\right\} & \text{if } w \in [\tilde{w}(Q), \infty), \\ w - p\left(\dot{\rho}(w)\right) & \text{if } w \in [0, \tilde{w}(Q)), \end{cases} \end{aligned} \tag{7}$$

being $\dot\rho(w)$, $\tilde v(Q)$ and $\tilde w(Q)$ implicitly defined by

$$w = p\left(\dot\rho(w)\right) + \dot\rho(w)\, p'\left(\dot\rho(w)\right), \qquad \frac{\tilde v(Q)^2}{Q} = p'\left(\frac{Q}{\tilde v(Q)}\right), \qquad \tilde w(Q) = \tilde v(Q) + p\left(\frac{Q}{\tilde v(Q)}\right).$$

See Figure 1 for a graphical representation of $\dot\rho(w)$, $\hat v(Q,w)$, $\check v(Q,w)$, $\tilde v(Q)$ and $\tilde w(Q)$.

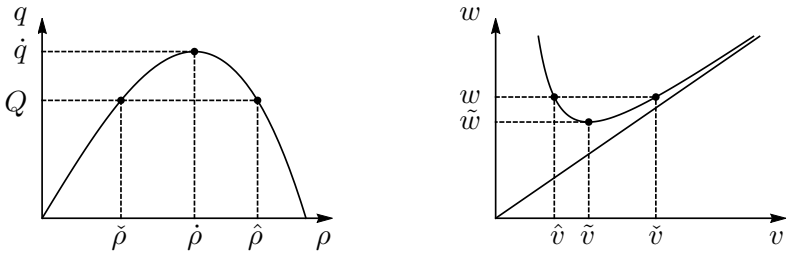

FIGURE 1. Left: the curve $q = [w - p(\rho)]\,\rho$ in the (ρ, q)-plane for a fixed value of w. We have $\hat\rho = \rho(\hat v, w)$ and $\check\rho = \rho(\check v, w)$, as in (2). Right: the curve $w = v + p(Q/v)$ in the (v, w)-plane for a fixed value of Q.

Definition 2.2 (The constrained Riemann solver: $\mathcal{RS}_Q$)**.** *Fix a constant $Q \in \mathbb{R}_+$. For any $W_\ell = (v_\ell, w_\ell), W_r = (v_r, w_r) \in \mathcal{W}$, we define $\mathcal{RS}_Q[W_\ell, W_r] \in C^0\left(\mathbb{R}_+; \mathbf{L}^1_{\rm loc}(\mathbb{R}; \mathcal{W})\right)$ as follows:*

- *if $(v,w)(t,x) = \mathcal{RS}[W_\ell, W_r](x/t)$ satisfies the constraint condition $[v\,\rho(v,w)](t, 0^\pm) \leqslant Q$, then*
$$\mathcal{RS}_Q[W_\ell, W_r] = \mathcal{RS}[W_\ell, W_r];$$
- *otherwise we let*
$$\mathcal{RS}_Q[W_\ell, W_r](\nu) = \begin{cases} \mathcal{RS}[W_\ell, \hat W(Q, w_\ell)](\nu), & \text{if } \nu < 0, \\ \mathcal{RS}[\check W(Q, w_\ell), W_r](\nu), & \text{if } \nu \geqslant 0, \end{cases}$$

where $\hat W(Q, w_\ell) = (\hat v(Q, w_\ell), w_\ell)$ and $\check W(Q, w_\ell) = (\check v(Q, w_\ell), w_\ell)$.

Remark 2.1. *The Riemann solver $\mathcal{RS}$ does not coincide with the one introduced in* [7]*, but it is tailored to meet the requirements of the numerical implementation. Indeed, the initial conditions for cases 1, 5, 6, and 7 in Definition 2.1 are either trivial or not physically relevant, as they involve jumps in the w variable in the vacuum. Nevertheless, these cases must be included for completeness in our numerical solver.*

In particular, this implies that the Riemann solver $\mathcal{RS}_Q$ does not coincide with the one introduced in [4]*. However, if $W_\ell \in \mathcal{W}_0$, then $(t,x) \mapsto \mathcal{RS}[W_\ell, W_r](x/t)$ satisfies the constraint condition simply because $\mathcal{RS}[W_\ell, W_r](0^\pm) = W_\ell \in \mathcal{W}_0$, and hence $\mathcal{RS}_Q[W_\ell, W_r] = \mathcal{RS}[W_\ell, W_r]$. As a consequence, in practice, $\mathcal{RS}_Q$ coincides with the Riemann solver introduced in* [4] *for the Riemann data that activate the constraint.*

3. The numerical method

In this Section, we introduce our numerical method. For all the simulations of this paper, we consider the classical prototype for the velocity offset

$$p(\rho) = v_{\rm ref}\left(\frac{\rho}{\rho_{\rm ref}}\right)^\gamma, \tag{8}$$

with $v_{\rm ref}$, $\rho_{\rm ref}$ and γ strictly positive parameters. In Section 5.1 we also consider

$$p(\rho) = v_{\rm ref}\left(\frac{\rho\,\rho_{\max}}{\rho_{\max} - \rho}\right)^\gamma, \tag{9}$$

which is used in [9, 8, 17].This allows to compare the effects of (8) and (9) on the dynamics. Observe that the velocity offset in (9) is only defined for $\rho \in [0, \rho_{\max})$ and is singular at $\rho_{\max}$.

3.1. **Glimm scheme motivation.** For any given $v_m, w_m, w_M \in \overline{\mathbb{R}}_+$ such that $0 \leqslant v_m \leqslant w_m < w_M$, the domain $\{(v, w) \in \mathcal{W} : v_m \leqslant v,\ w_m \leqslant w \leqslant w_M\}$ is an invariant domain of $\mathcal{RS}$. Therefore, the solution of any (unconstrained) Cauchy problem associated with the ARZ model is confined for all times $t \in \overline{\mathbb{R}}_+$ in the invariant region corresponding to its initial condition $x \mapsto (\bar{v}(x), \bar{w}(x))$, that is to $v_m = \inf_{\mathbb{R}}\{\bar{v}\}$, $w_m = \inf_{\mathbb{R}}\{\bar{w}\}$ and, $w_M = \sup_{\mathbb{R}}\{\bar{w}\}$.

However, as observed in [11], such domains do not correspond in general to convex regions in the plane of conservative variables, ρ and y. Therefore, conservative numerical schemes that average ρ and y, such as the Godunov scheme, fail to satisfy the maximum principle for the Riemann invariants of the ARZ system (and, consequently, for the ADR system as well). Typically, one may observe spurious oscillations in the approximation of Riemann problems whose solution consists of a single contact discontinuity (which means that the velocity v was constant in the initial condition), see [11] for a detailed discussion. In [11] the authors propose a transport-equilibrium scheme that overcomes this difficulty and suggests two additional ways to obtain the same result. The first one consists in using a finite volumes scheme averaging ρ and v but leads to complicate upgrade formulas. The second direction is to use the Glimm scheme, which has been successfully done in [10] for the ARZ model. In particular, the results in [10] prove that the Glimm scheme reproduces correctly the vacuum formation for the ARZ system.

In the ARZ model, the vacuum may appear in finite time starting from non-vacuum initial conditions, see Case 10 in Definition 2.1. We stress that the Riemann solver $\mathcal{RS}$ in this case plays the special role of selection criterion, as the system of conservation laws degenerates at the vacuum and, from the PDE's point of view, it admits in principle two different entropy admissible solutions, as pointed out in [7, 37]. This issue is not completely addressed in [11], where the authors consider the ARZ model with the velocity offset $p(\rho) = v_{\text{ref}} \ln(\rho/\rho_{\text{ref}})$. Since this function is not defined at $\rho = 0$, they can not explore the case of vacuum opening, see also [10, Remark 2] for more details on this choice. However, the finite volumes numerical scheme introduced in [6] for the ADR model, which essentially relies on [11] for the treatment of the contact discontinuities, fails to capture the prescribed solution with a velocity offset of the form (8).

For completeness, we recall in the next lemma the invariant domains for the constrained Riemann solver.

Lemma 3.1. *Given any triple $0 \leqslant v_m \leqslant w_m < w_M$ which satisfies one of the following conditions*

$$\text{(i) } w_M \leqslant \tilde{w}, \quad \text{(ii) } w_M > \tilde{w} \text{ and } v_m \geqslant \check{v}(Q, w_M), \quad \text{(iii) } w_M > \tilde{w} \text{ and } v_m \leqslant \hat{v}(Q, w_M),$$

the set $\{(v, w) \in \mathcal{W} : v \geqslant v_m,\ w \in [w_m, w_M]\}$ is an invariant region for $\mathcal{RS}_Q$.

3.2. **Description of the scheme.** We describe here the Glimm scheme for the approximation of the ADR model, namely the ARZ system subject to point constraints on the density flux. We denote by N the number of mesh cells in the computational domain and let Δx be the space step. We introduce the points $x_{j+1/2} = j\,\Delta x$, the cells $\mathcal{C}_j = [x_{j-1/2}, x_{j+1/2})$ and the cell centers $x_j = (j - 1/2)\,\Delta x$ for $j \in [\![1, N]\!]$. We denote by j_c the index such that $x_{j_c+1/2}$ is the location of the constraint. For any integer $n \geqslant 0$ and for any $j \in [\![1, N]\!]$, the goal is to compute W_j^n, the approximated value of $W(t^n, x_j)$, where $(t^n)_n$ is recursively defined by

$$t^0 = 0, \qquad\qquad t^{n+1} = t^n + \Delta t_{n+1},$$

with the time step $(\Delta t_n)_n$ given below. We start by defining

$$W_j^0 = (\bar{v}(x_j), \bar{w}(x_j))\,.$$

For a fixed integer $n \geqslant 1$, assuming that W_j^n is given for any $j \in [\![1, N]\!]$, we define the time step Δt_{n+1} so that the following CFL condition is satisfied:

$$\Delta t_{n+1} = \frac{C_{\text{cfl}}\, \Delta x}{S^n_{\max}}.$$

Above, $S^n_{\max}$ is the maximum wave speed (in absolute value) present in the whole domain at time t^n, and the CFL coefficient C_{cfl} satisfies $0 < C_{\text{cfl}} \leqslant 1/2$. We choose $C_{\text{cfl}} = 1/2$ for all the simulations of this paper. The next time discretization is given by $t^{n+1} = \sum_{i=1}^{n+1} \Delta t_i$. We use the following procedure to compute W_j^{n+1}:

- As in [13, 36], we pick quasi-randomly a number $\theta^n \in [0, 1]$ by considering the van der Corput sequence $(\theta^n)_n$ defined by

$$\theta^n = \sum_{k=0}^{m} i_k\, 2^{-(k+1)},$$

  where $(i_0, \dots, i_m)$, with $i_k \in \{0, 1\}$, is the binary expansion of the integer n, namely

$$n = \sum_{k=0}^{m} i_k\, 2^k.$$

- Define $\Delta\nu_{n+1} = \Delta x/\Delta t_{n+1}$. The updated solution is then computed as follows:

$$W_j^{n+1} = \begin{cases} \mathcal{RS}[W_{j-1}^n, W_j^n]\,(\theta^n \Delta\nu_{n+1})\,, & \text{if } 0 \leqslant \theta^n < 1/2, \\ \mathcal{RS}[W_j^n, W_{j+1}^n]\,((\theta^n - 1)\Delta\nu_{n+1})\,, & \text{if } 1/2 \leqslant \theta^n \leqslant 1, \end{cases} \qquad j \notin \{j_c, j_{c+1}\}$$

$$W_{j_c}^{n+1} = \begin{cases} \mathcal{RS}[W_{j_c-1}^n, W_{j_c}^n]\,(\theta^n \Delta\nu_{n+1})\,, & \text{if } 0 \leqslant \theta^n < 1/2, \\ \mathcal{RS}_Q[W_{j_c}^n, W_{j_c}^n]\,((\theta^n - 1)\Delta\nu_{n+1})\,, & \text{if } 1/2 \leqslant \theta^n \leqslant 1, \end{cases}$$

$$W_{j_c+1}^{n+1} = \begin{cases} \mathcal{RS}_Q[W_{j_c}^n, W_{j_c+1}^n](\theta^n \Delta\nu_{n+1}), & \text{if } 0 \leqslant \theta^n < 1/2, \\ \mathcal{RS}[W_{j_c+1}^n, W_{j_c+2}^n]((\theta^n - 1)\Delta\nu_{n+1}), & \text{if } 1/2 \leqslant \theta^n \leqslant 1. \end{cases}$$

We observe that, on the one hand, the scheme does not introduce any numerical viscosity, which means, in particular, that the size of jump discontinuities is computed exactly. On the other hand, however, the location of jumps is detected "up to one cell." The resulting error is very small for fine meshes but is unavoidable, see Remark 5.1 for further discussion.

3.3. **Remarks on the implementation of the method.** In the Riemann solver implementation, we could in principle pick different pairs of variables: the physical variables (ρ, v), the conservative ones (ρ, y), the Riemann invariants (v, w), or even (ρ, q).

This last choice would make our simulations very intuitive, but would also be very delicate for extremely low densities because there is no definite map to recover the values of the Riemann invariants starting from $\rho = 0$, $q = 0$.

We perform our simulations in physical variables as they are still relatively easy to compare to available data, and can be translated into conservative variables or to Riemann invariant coordinates in all situations. Notice, however, that in order to avoid spurious oscillations at the constraint location, our implementation keeps track of all the state variables ρ, v, q, w and $p(\rho)$.

Indeed, the Riemann solver $\mathcal{RS}_Q$ is deduced by assuming the conservation of w and the maximization of q at the constraint location. Namely, whenever the constraint is active, $q = Q$. Floating-point calculations for the estimation of physical variables may induce tiny errors in the flux estimation, as $q = \rho\, v$. Thus, we may fail to realize the condition $\rho\, v(t, 0^-) = \rho\, v(t, 0^+) = Q$, and this would lead the Glimm scheme to oscillate between constrained and unconstrained Riemann solver at each time step.

Unless otherwise specified, all the simulations presented in this paper are made by imposing Neumann conditions at the boundary of the computational domain, and with a velocity offset of the form (8) and parameters' values $v_{\text{ref}} = 1$, $\rho_{\text{ref}} = 1$ and $\gamma = 4$, that is

$$p(\rho) = \rho^4. \tag{10}$$

4. Validation of the numerical scheme

4.1. **Numerical convergence.** To validate the numerical convergence of the Glimm scheme, we study the evolution of the relative ℓ^1-error between numerical solutions and explicit exact solutions for varying mesh sizes. The comparison is made for two constrained Riemann problems (6), one of which leads to the appearance of the vacuum in the solution. The exact solutions are provided by the Riemann solvers described in Section 2. In both cases, the constraint is located at $x = 0$ and the upper bound for the density flux is $Q = 0.1$.

Using the notations introduced in Section 3.2, for any given state variable $u \in \{\rho, v, q, w, p\}$, we call u_j^n the approximate value on the cell $\mathcal{C}_j$ at time t^n of $u(t^n, x_j)$. Thus the relative ℓ^1-error at time t^n for u is

$$E_{\ell^1}^n = \left(\sum_{j\in\mathbb{Z}} \left|u(t^n, x_j) - u_j^n\right|\right) \Big/ \left(\sum_{j\in\mathbb{Z}} |u(t^n, x_j)|\right). \tag{11}$$

Example 4.1. *Consider the Riemann problem* (6) *with*

$$(\rho_\ell, v_\ell) = (0.65, 0.10), \qquad (\rho_r, v_r) = (0.20, 0.75). \tag{12}$$

The solution consists of the juxtaposition of a rarefaction wave of negative speed, a stationary non-classical shock induced by the flux constraint, a rarefaction wave leading to the vacuum, and finally a contact discontinuity. The exact solution and the approximated solution obtained using the Glimm scheme at time $t = 1$ are presented in Figure 2. According to this figure, the exact solution is well captured by the Glimm scheme. The convergence rate is 0.96 *for the density and* 1.00 *for the velocity, see Figure 4a. We observe in Figure 2c that w in the vacuum is computed according to the Riemann solver $\mathcal{RS}$ presented in Definition 2.1.*

Example 4.2. *Consider the Riemann problem* (6) *with*

$$(\rho_\ell, v_\ell) = (0.50, 1.10), \qquad (\rho_r, v_r) = (0.20, 0.35). \tag{13}$$

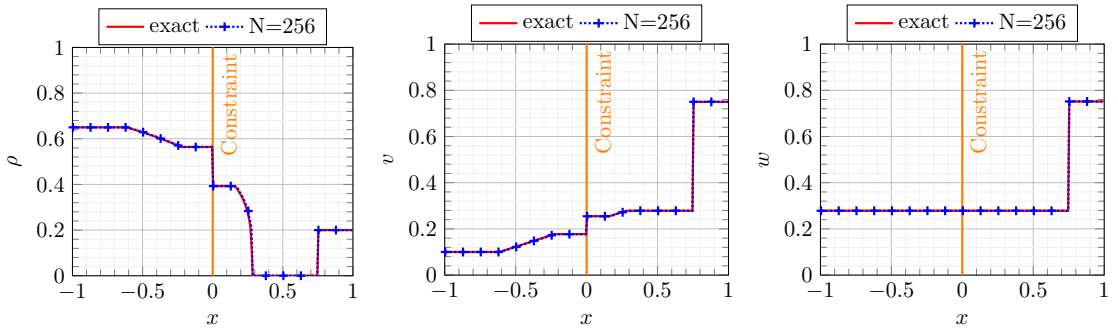

(A) Density: ρ (B) Velocity: v (C) Generalized momentum: w

FIGURE 2. Comparison between the exact solution, in red, and the numerically computed solution, in blue, at time $t = 1$ for the Riemann problem (6) with velocity offset (10), initial data (12), and $Q = 0.1$ located at $x = 0$ (orange line). The simulation using the Glimm scheme is performed using a uniform grid of $N = 256$ mesh cells.

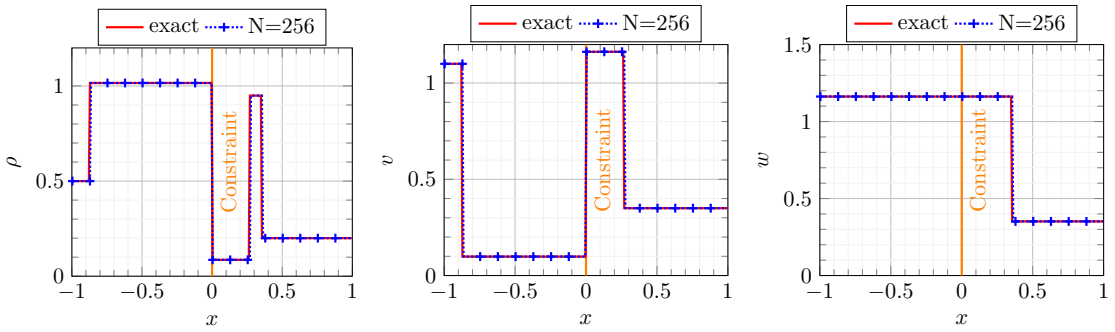

(A) Density (B) Velocity (C) Generalized momentum: w

FIGURE 3. Comparison between the exact solution, in red, and the numerically computed solution, in blue, at time $t = 1$ for the Riemann problem (6) with velocity offset (10), initial data (13), and $Q = 0.1$ located at $x = 0$ (orange line). The simulation using the Glimm scheme is performed using a uniform grid of $N = 256$ mesh cells.

The exact solution consists in a shock of negative speed, followed by a stationary non-classical shock, induced by the flux constraint, then a shock of positive speed and finally a contact discontinuity. The exact solution and the approximated solution obtained using the Glimm scheme at time $t = 1$ *are presented in Figure 3. According to this figure, the exact solution is well captured by the Glimm scheme. The convergence rate is* 0.90 *for the density and* 0.91 *for the velocity, see Figure 4b.*

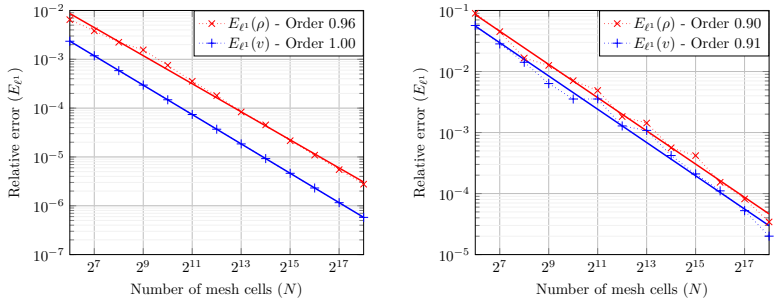

(A) Glimm scheme convergence analysis for the Riemann problem (6) with initial data (12), and $Q = 0.1$. The convergence rate is 0.96 for the density and 1.00 for the velocity.

(B) Glimm scheme convergence analysis for the Riemann problem (6) with initial data (13), and $Q = 0.1$. The convergence rate is 0.91 for the density and 0.90 for the velocity.

FIGURE 4. Convergence analysis: Relative error in ℓ^1-norm (see formula (11)) for the density ρ and the velocity v with respect to the number of mesh cells N.

4.2. **Partial validation of the scheme for Lipschitz continuous and non-local constraints.** In the following examples, we consider the special situation in which the Lagrangian marker of the initial data is constant. More specifically, the initial data are

$$(\bar{\rho}, \bar{v})(x) = \begin{cases} (1,1), & \text{if } x \in [a,b], \\ (0,2), & \text{otherwise,} \end{cases} \tag{14}$$

where $[a, b] \subset \mathbb{R}$. Observe that $\bar{w} = 2$ everywhere, including in the vacuum. As usual we consider the velocity offset (10). In this setting the dynamics described by the ARZ model is the same as the one captured by the first order LWR model [27, 31] with flux function $f(\rho) = \rho\,(w - p(\rho)) = \rho\,(2 - \rho^4)$. The (theoretical and numerical) convergence of finite volumes approximations for the constrained LWR model is well known, even when the level of the constraint is Lipschitz continuous in time and depends non-locally on the solution itself, see [2, 12].

This allows us to partially validate our Glimm type scheme by comparing the density component of our solution with the solution of the constrained LWR model computed via the convergent finite volumes type scheme in [2], for a wide range of constraints functions Q.

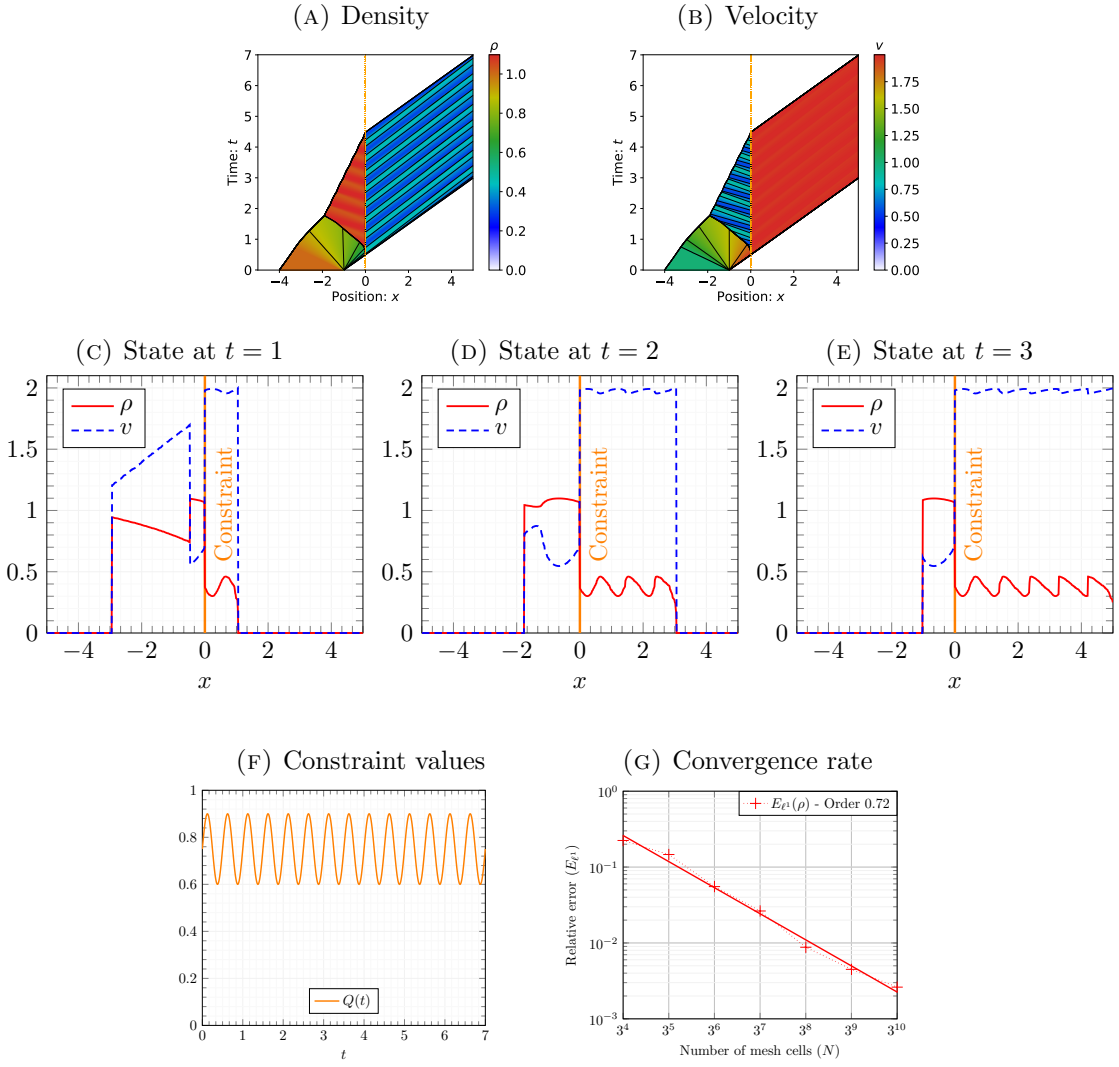

FIGURE 5. Numerical solution obtained by the Glimm scheme of the ADR model (1) with initial data (14) with $[a, b] = [-4, -1]$, and time dependent constraint $Q(t)$ represented in sub-Figure 5f and given by equation (15). Figures 5a and 5b represent respectively the heat map of the density and the velocity in space and time. Figures 5c-5e represent the densities and the velocities at different times. Figure 5g illustrates the convergence rate toward the solution of the constrained LWR model.

Example 4.3. *Consider the ADR model* (1) *with initial data* (14) *with* $[a,b]=[-4,-1]$ *and the time dependent constraint*

$$Q(t)=\alpha+\beta\sin\left(\frac{2\pi t}{\theta}\right) \qquad \text{with } \alpha=0.75,\ \beta=0.15,\ \text{and } \theta=0.5. \tag{15}$$

For the discretization, the domain is $[-5,5]$ *and the number of mesh cells is* $N=5000$. *Figure 5 represents the heat maps of the numerical solution obtained by the Glimm type scheme, and the snapshots at times* $t=1$, $t=2$ *and* $t=3$. *The numerical convergence rate of the relative* ℓ^1*-error between our solution and the constrained LWR solution is* 0.72, *as shown in Figure 5f.*

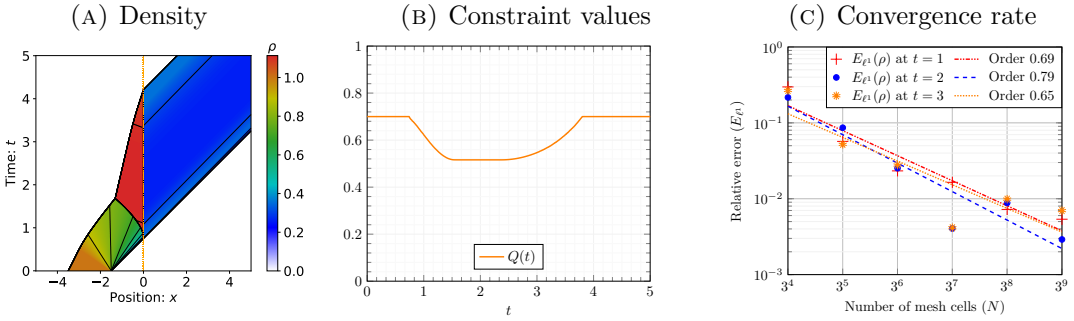

FIGURE 6. Numerical solution obtained by the Glimm scheme of the ADR model (1) with initial data (14) with $[a,b]=[-3.5,-1.5]$. The non-local constraint $Q(t)$ given by equation (16) and is a decreasing function of the weighted averaged density in the local upstream area of the constraint, namely on $[-1,0]$. Figure 6a represents the heat map of the density in space and time. Figure 6b represents the time evolution of the constraint. Figure 6c represents the convergence rate for different times: at $t=1$ when the constraint value is decreasing, at $t=2$ when the constraint is at its lower level, and at $t=3$ when the constraint is returning to its original level.

Example 4.4. *Consider the ADR model* (1) *with initial data* (14) *with* $[a,b]=[-3.5,-1.5]$ *and the non-local constraint*

$$Q(t)=\begin{cases} q_0 & \text{if } \xi(t)\leqslant\xi_0,\\ \alpha\,\xi(t)+\beta & \text{if } \xi_0<\xi(t)<\xi_1,\\ q_1 & \text{if } \xi(t)\geqslant\xi_1,\end{cases} \quad \text{with } \begin{cases} q_0=0.7,\ \xi_0=0.5,\ \alpha=\frac{q_1-q_0}{\xi_1-\xi_0},\\ q_1=0.4,\ \xi_1=1.5,\ \beta=q_1-\frac{q_1-q_0}{\xi_1-\xi_0}\,\xi_1,\end{cases} \tag{16}$$

where

$$\xi(t)=\frac{\int_\Omega \rho(t,x)\,\varphi(x)\,\mathrm{d}x}{\int_\Omega \varphi(x)\,\mathrm{d}x} \qquad \text{with } \Omega=[-1,0],\ \varphi(x)=2x+2.$$

Figure 6a represents the heat map of the numerical solution obtained by the Glimm type scheme, and Figure 6b the evolution of the constraint level in time. Figure 6c presents the numerical convergence rate of the relative error between our solution and the constrained LWR solution at different times: it is 0.69 *at* $t=1$, *when the constraint value is decreasing,* 0.79 *at* $t=2$ *when the constraint is stable at its lower level, and* 0.65 *at* $t=3$ *when the constraint is returning to its original level.*

Observe that Q is continuous because $\rho\in C^0\left(\overline{\mathbb{R}}_+;\mathbf{L}^1_{\mathrm{loc}}(\mathbb{R};\overline{\mathbb{R}}_+)\right)$. In B we consider the case of a non-local constraint Q that is discontinuous even in the case $\rho\in C^0\left(\overline{\mathbb{R}}_+;\mathbf{L}^1_{\mathrm{loc}}(\mathbb{R};\overline{\mathbb{R}}_+)\right)$.

5. Qualitative behavior of the ADR model

In this Section, we provide a number of numerical experiments showing that, starting from the ADR model, we can reproduce the qualitative behavior of traffic observed in real situations and, in particular, characteristic phenomena associated to the presence of obstacles and bottlenecks, such as phantom jams, capacity drop, Braess' paradox and Faster is Slower effect.

5.1. **Phantom jams.**

The "phantom jam" effect refers to a phenomenon empirically observed in traffic flow, where a temporary, localized slowdown in traffic (typically, starting with a single vehicle overbraking or changing lane unexpectedly) causes a chain reaction of deceleration and congestion among other vehicles, creating a "phantom" traffic jam propagating backwards through the traffic stream.

The traffic flow disruption at the origin of the "phantom jam" can be modeled by a point constraint on the flow. Thus the ADR model is well-suited to reproduce this mechanism.

We consider a highway with heavy, not very fast traffic, and imagine that at $t = \bar{t}$ a vehicle, called B, suddenly brakes, while the vehicles around it do not modify their speed. Immediately after, the vehicle B recovers its previous velocity and blend in the traffic flow, so that we do not follow further its trajectory. The situation is similar to the case in which a bus or a truck is seen as a moving obstacle in the traffic, see [18, 19, 35, 34], but only for a very short time. For the simulation, we represent the braking vehicle by a local point constraint, which stays active on a brief time interval.

Figure 17 represents the traffic flow dynamic heat-map in time and space associated to this situation. In the simulation the constraint is located at $x = 0$ and activated for $t \in [1.25, 1.35]$ with the value $Q = 0.1$. The initial data consists of several blocks with a common velocity but different densities, so that different values of w are involved

$$\big(\bar{\rho}(x), \bar{v}(x)\big) = \begin{cases} (0.80, 1), & \text{if } x \in [-4, -3.5], \\ (0.75, 1), & \text{if } x \in [-3.5, -3], \\ (0.70, 1), & \text{if } x \in [-3, -2.5], \\ (0.65, 1), & \text{if } x \in [-2.5, -2], \\ (0.60, 1), & \text{if } x \in [-2, -1.5], \\ (0.50, 1), & \text{if } x \in [-1.5, -1], \\ (0, 0), & \text{otherwise.} \end{cases} \tag{17}$$

For the discretization, the domain is $[-5, 5]$ and the number of mesh cells is $N = 5000$. According to Figure 7, a jam is created in the upstream flow during the period of constraint activation. Then, at the front of the congestion, a rarefaction occurs whereas in the upstream flow the "phantom jam" appears. The "phantom jam" creation begins at $t = 1.35$, then the congestion propagates to each block of the initial data and reaches the tail of the group of vehicles (i.e. the left boundary of the support of $\rho(t, x)$) at $t = 3.25$.

Figure 8 is obtained using the same setting except for the velocity offset. Instead of using a power law, see equation (10), we consider the singular law given by (9), with $v_{\text{ref}} = 0.05$, $\rho_{\text{ref}} = 1$ and $\gamma = 4$. In this case, the "phantom jam" congestion propagates much faster. This behavior is induced by the singularity of the velocity offset when the density reaches the threshold ρ_{ref} leading to infinite propagation speed for shocks.

5.2. **Capacity drop.**

The capacity drop effect refers to the situation in which the empirically measured value of the density flux on a road section is lower than expected for the given traffic status. The flow rate reduction causes are diverse, but likely involve the density and the velocity of vehicles in the surrounding area of the constraint. For example, the change of line or the last-minute braking report might be involved in the capacity drop effect, see [32]

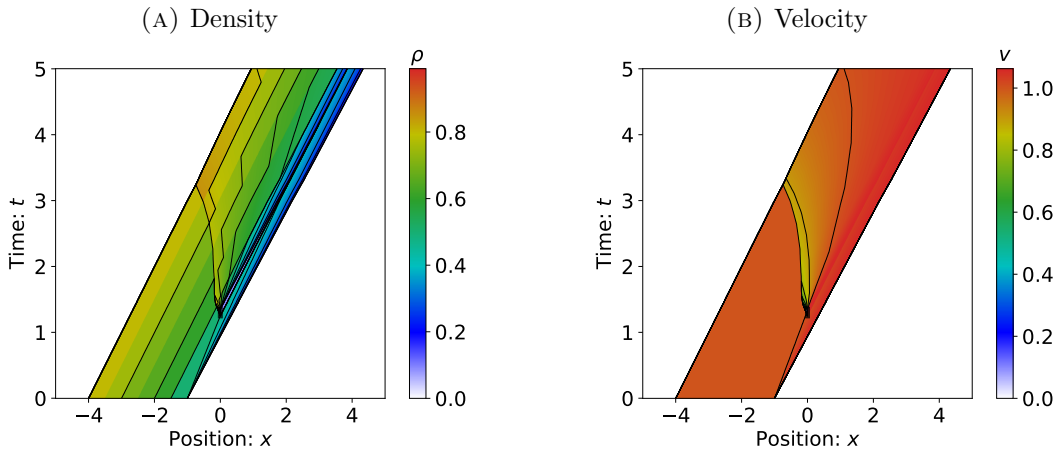

FIGURE 7. Time and space dynamics of the phantom jam created by a constraint at $x = 0$ activated for $t \in [1.25, 1.35]$ with $Q = 0.1$. Figure 7a and Figure 7b represent the evolution of the density and of the velocity, respectively. The initial data is given in (17). The velocity offset is the power law, see (10).

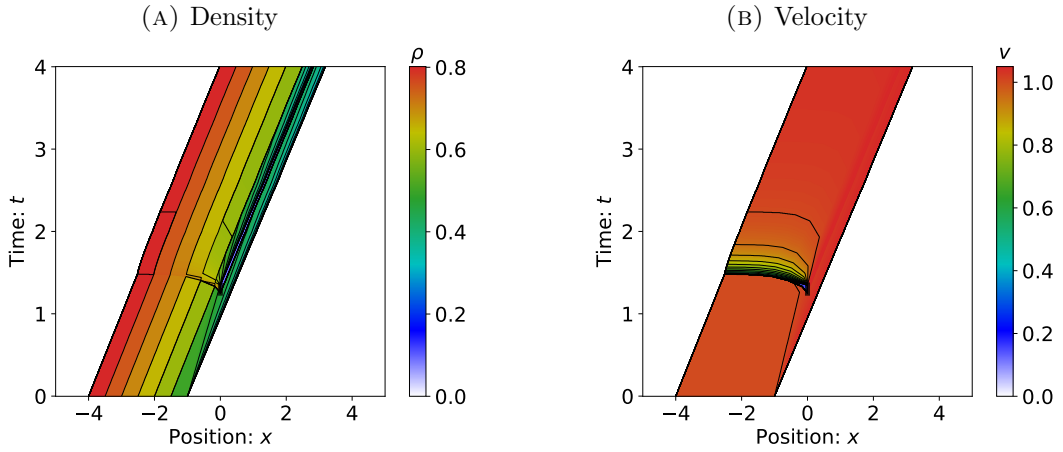

FIGURE 8. Time and space dynamics of the phantom jam created by a constraint at $x = 0$ activated for $t \in [1.25, 1.35]$ with $Q = 0.1$. Figures 8a and 8b represent the evolution of the density and of the velocity, respectively. The initial data is given in (17). The velocity offset is the singular law given in (9) with $v_{\text{ref}} = 0.05$, $\rho_{\text{ref}} = 1$ and $\gamma = 4$.

for a more detailed presentation of the phenomenon and its causes. In [1, 6, 2] the capacity drop effect is modeled by imposing a constraint Q localized at the point at which the loss of efficiency if observed, and depending (possibly in a non-local way) on the upstream traffic density or on the flux registered from captors over a given interval of time.

Our Glimm type scheme allows to obtain solutions for an enhanced version of the ADR model, in which the constraint value depends non-locally on the density component of the solution; see Example 4.4 and B for the case in which $\bar{w}$ is constant. The results for more general initial conditions are similar.

5.2.1. *Faster is Slower effect (FIS).* To our knowledge, the FIS effect, also known as "freezing by heating", [33], was first formalized in [23] in the context of the room evacuation problem. The authors studied the evacuation time as a function of the maximal velocity reached by pedestrians, and they shown that there exists an optimal velocity (well lower than the highest attainable by single pedestrians) for which the evacuation time attains a minimum. Following the studies above, the curve representing the evacuation time as a function of the average velocity takes a characteristic shape, see [30, Figure 1c]. Recently it has been shown how the FIS effect takes place in a variety of phenomena, such as in vehicular traffic, see [20] and the references therein. In this setting, a higher speed results in more pronounced breaking in the presence of road structure modifications, such as lane merging or obstacles, and facilitates the appearance of phantom jams.

In this section we investigate the ability of the ADR model to reproduce the FIS effect. We focus our attention to a non-local constraint of the form (16), as the model in its original form (with piece-wise constant in time, given constraint levels) does not suffice. This is not really surprising, as heuristically the FIS effect is strongly connected to the capacity drop, in the sense that it also relates to a lack of self-organization upstream the location of a bottleneck.

The spatial domain in the next numerical experiments is set to $[-3.1, 0.1]$, and subdivided using a uniform mesh grid made of $N = 16384$ mesh cells. As for other simulations, the velocity offset is (10). The non-local constraint on the density flux is located at $x = 0$ and its level is given by equations (16), with the parameters provided in Table 1.

The initial condition consists of two uniform blocks of constant density, which share the same initial constant velocity. While the values of the density are the same over all simulations, the common value of the initial velocity varies in $[0.25, 2.5]$ by step of 0.01. For each of these values we record the egress time, i.e. the first time at which the portion of the domain upstream $x = 0$ is empty.

We conducted the experiment twice, permuting the order of the blocks, so that the two initial configurations for the density are

$$\bar\rho_A(x) = \begin{cases} 1.2, & \text{if } x \in [-3,-2], \\ 0.8, & \text{if } x \in [-2,-1], \\ 0, & \text{otherwise,} \end{cases} \qquad \bar\rho_B(x) = \begin{cases} 0.8, & \text{if } x \in [-3,-2], \\ 1.2, & \text{if } x \in [-2,-1], \\ 0, & \text{otherwise.} \end{cases} \tag{18}$$

Figure 9 presents the results. For both initial densities, there is an optimum initial speed, which is $\bar v = 0.75$ for ρ_A and $\bar v = 0.78$ for ρ_B, leading to minimal egress times $T^A_{\text{op}} = 6.313$ and $T^B_{\text{op}} = 6.525$. Thus, even if the variation of the egress time follows similar patterns, the computed critical values depend on the initial configuration.

Remark 5.1. *Small oscillations can be observed in Figure 9. These oscillations are induced by the random sampling used in the Glimm scheme. Using a very refined mesh grid allows for reducing these oscillations and capturing more precisely the egress time. However, taking more refined mesh grids significantly increases the computational time. Thus, the choice of taking* $N = 16384$ *mesh cells allows us to keep the computational time reasonable while capturing the egress time with sufficient accuracy to assess the impact of the initial velocity.*

In Figure 10 we compare the heat-maps of three solutions corresponding to the initial condition $\bar\rho_A$ for the density, see (18), and 0.5, 0.75 and 1.13 respectively for the velocity. As mentioned above, $\bar v = 0.75$ allows to attain the minimal egress time, T^A_{op}. The other initial velocity values are chosen as they both lead to egress time $T = 105\%\, T^A_{\text{op}}$. We can see that the corresponding dynamics are different: The fact that the constraint reaches its lowest value sooner and remains there for a time span about 60% longer compensates the possible advantage coming from a higher initial velocity, enlightening the FIS effect, see also Figure 11.

Parameter	q_0	q_1	ξ_0	ξ_1	Ω	$\varphi(x)$
Value	0.75	0.25	0.5	1.0	$[-1, 0]$	$x \mapsto 2x + 2$

TABLE 1. Settings for the non-local constraint used for the simulations in Figure 9. The expression of the non-local constraint is given by equations (16).

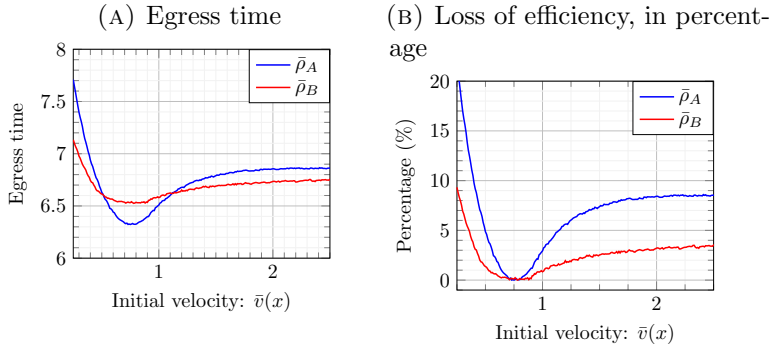

FIGURE 9. Illustration of the "Faster is Slower" effect with a non-local constraint for the initial data in (18). Figure 9a: egress time with respect to the initial velocity. Figure 9b: percentage of efficiency loss compared to the optimum, namely $100\,\frac{T - T_{\text{op}}}{T^A_{\text{op}}}$.

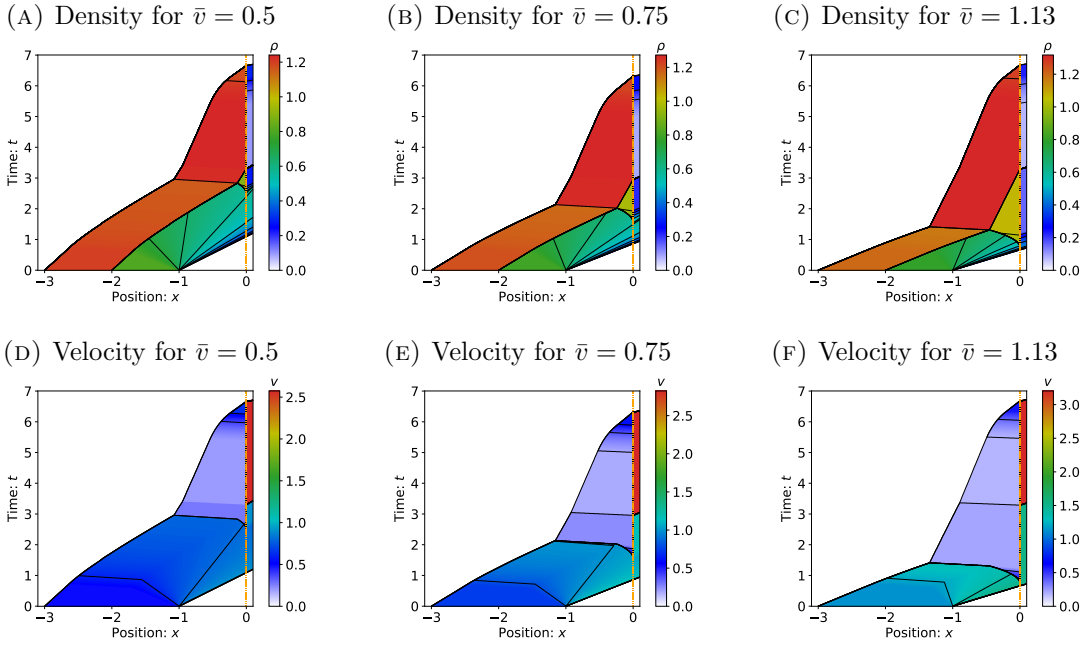

FIGURE 10. Solutions comparison in space and time for different values of initial velocity when the initial density is ρ_A given by (18). The above three columns correspond to the initial velocities $\bar{v} = 0.5$, $\bar{v} = 0.75$ (which minimizes egress time), and, $\bar{v} = 1.13$. For the solutions in the first and the third columns, the egress time is about $6.629 \approx 105\%\, T^A_{\text{op}}$.

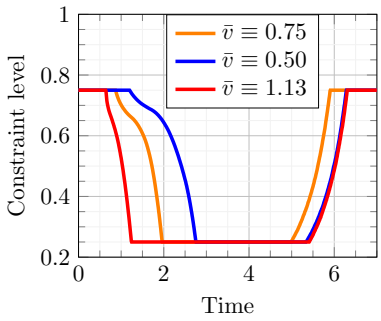

FIGURE 11. Evolution of the constraint $Q(t)$ for different values of the initial speed.

5.3. **Braess' paradox with a non-local constraint.** This section investigates the model's ability to reproduce a second effect intimately related to capacity drop, which we call here Braess' paradox. This terminology may lead to confusion, and need some explanation. The name "Braess' paradox" appeared first in the description of vehicular traffic on a network, to describe the situation in which if one of the road-branches is not accessible to the agents, the average flow lightens in the remaining ones. In the setting of pedestrian traffic, however, "Braess' paradox" refers to the situation in which a (small) obstacle, located in the vicinity of an exit, allows for faster evacuation because it prevents peaks of high density and, therefore, reduces the capacity drop. In this paper we borrow the latter meaning, even if we are concerned with vehicular traffic, because we limit our attention to the dynamics on a single road.

In this experiment, we consider that the level of the upstream constraint is constant and given, while the level of the downstream constraint depends non-locally from the average upstream weighed density of vehicles. Essentially, we try to model the situation in which the presence of an obstacle before a toll plaza reduces the taxing behavior at the gates. Our goal is to show that it is possible to optimize the position x_Q and the level Q of the (constant) upstream constraint so to minimize the egress time.

The computational domain for our experiences is $[-0.1, 5.1]$ and it is subdivided in $N = 10400$ mesh cells. As in previous simulations, the velocity offset is given by (10). We choose initial data consisting of two uniform blocks with different values for w

$$\big(\bar{\rho}(x), \bar{v}(x)\big) = \begin{cases} (1.2, 1.0), & \text{if } x \in [0, 1], \\ (0.8, 1.0), & \text{if } x \in [1, 2], \\ (0, 0), & \text{otherwise.} \end{cases} \tag{19}$$

The downstream constraint is placed at $x = 5.0$, is non-local and takes the form given by equations (16), with the parameters in Table 2.

We perform simulations for values of Q varying in $[0.2, 0.8]$ by step of 0.01, and locations x_Q varying in $[3, 4.9]$ by step of 0.02. We present our results in Figure 12. To illustrate the

Parameter	q_0	q_1	ξ_0	ξ_1	Ω	$\varphi(x)$
Value	0.5	0.25	0.5	1.0	$[4, 5]$	$x \mapsto 2x - 8$

TABLE 2. Settings for the non-local downstream constraint used for the simulations presented in Figure 12. The expression of the non-local constraint is given by equations (16).

effect of the upstream constraint, Figures 12a, 12b and 12c show the percentage of gain or loss in the egress time corresponding to different values of x_Q and Q. Let T_{ref} be the egress time

without the upstream constraint. The quantity we represent by the colours on the heat-map and on the vertical axes of Figures 12a and 12b, is

$$100\,\frac{T(x_Q,Q)-T_{\text{ref}}}{T_{\text{ref}}}.$$

The green cross on the heat-map represents the optimum location and the value for the upstream constraint. For this setting the optimum is reached at $x_Q = 4.1$ and $Q = 0.5$. According to this heat-map, however, there is a wide range of values and positions (i.e. dark blue area) for which adding the upstream constraint significantly reduces the egress time.

Observe that the optimal value for the constraint corresponds to the maximal capacity of the downstream constraint. Besides, according to Figure 12b and 12c the egress time is more sensitive to the value of constraint Q than to its position x_Q. Indeed, according to Figure 12b, slight variations of the constraint position around the optimum have limited impact on the percentage of gain even for constraint values that differ from the optimum. Conversely, according to Figure 12c, slight variations of the constraint value around the optimum significantly reduce the gain. These Figures also show that adding an upstream constraint improves the egress time as long as $Q \geqslant 0.3$. In a nutshell, our model suggests that the upstream constraint value must be carefully picked, but a good guess is to pick the value of the maximal capacity of the downstream constraint and then the position of the upstream constraint can be chosen more roughly.

Remark 5.2. *These heuristic conclusions are obtained for a given initial data and downstream constraint. The optimization process obviously must be carried out from scratch for different settings and, in particular, if one want to use a different kind of downstream constraint.*

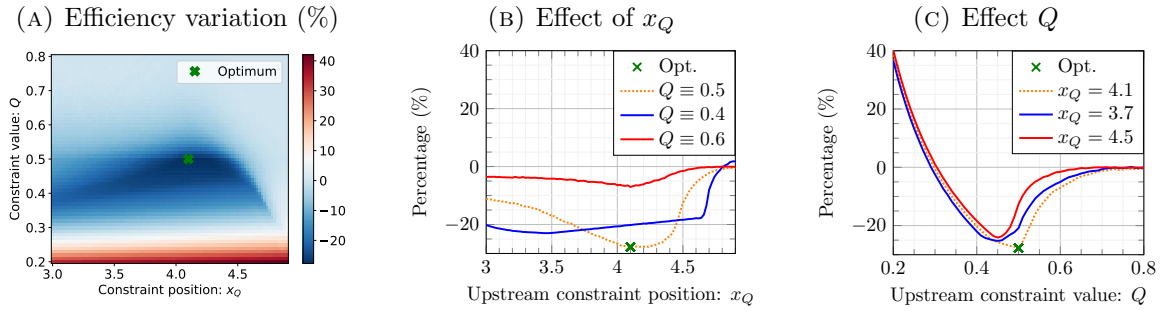

FIGURE 12. This figure illustrates the occurrence of Braess' paradox as described in Section 5.3 with initial data (19). Figure 12a shows the percentage of efficiency gain or loss relative to the absence of the upstream constraint, depending on the upstream constraint position x_Q and level Q. Figures 12b and 12c highlight, respectively, the effect of x_Q and Q on the percentage of efficiency gain or loss relative to the absence of the upstream constraint for different fixed values of Q (i.e. horizontal slices of Figure 12a) and for different positions of the constraint x_Q (i.e. vertical slices of Figure 12a).

We also consider the initial data obtained by switching the two blocks present in (19), that is

$$\big(\bar\rho(x),\bar v(x)\big) = \begin{cases} (0.8,1.0), & \text{if } x\in[0,1],\\ (1.2,1.0), & \text{if } x\in[1,2],\\ (0,0), & \text{otherwise.}\end{cases} \tag{20}$$

The results are presented in Figure 13. We can see that in this case, even if the curves have overall a similar shape, the dark blue region in the heat-map is thinner next to the optimal

value, which means that the dynamics is less stable. Nevertheless, the optimum for the upsteam constraint level is $Q = 0.49$, which almost corresponds to the highest level (ie. 0.5) of the downstream constraint.

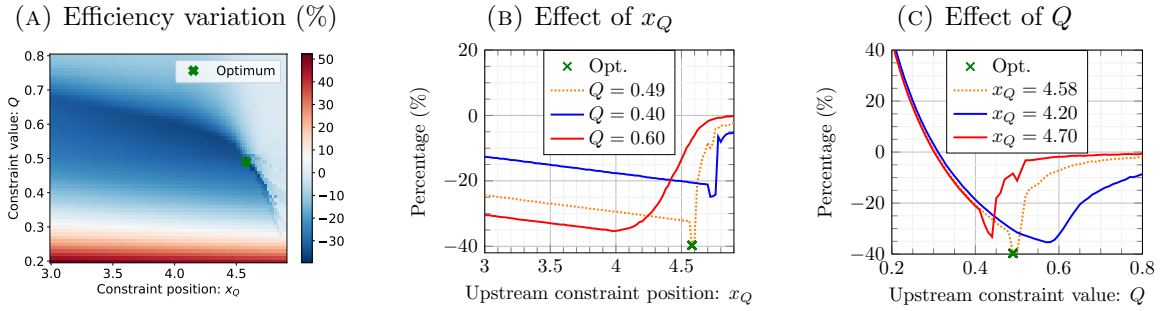

FIGURE 13. This figure illustrates the occurrence of Braess' paradox as described in Section 5.3 with initial data (20). Figure 13a show the percentage of efficiency gain or loss relative to the absence of the upstream constraint, depending on the upstream constraint position x_Q and level Q. Figure 13b and Figure 13c highlight, respectively, the effect of x_Q and of Q on the percentage of efficiency gain or loss relative to the absence of the upstream constraint for different fixed values of Q (i.e. horizontal slices of Figure 13a) and for different positions of the constraint x_Q (i.e. vertical slices of Figure 13a).

5.4. **A bridge with bounded carrying capacity.** One of the advantages of second order versus first order models is that they naturally represent the co-existence in the road of different kinds of vehicles (or drivers' attitudes). Classically, we relate the Lagrangian marker w in the ARZ model to the length-size of vehicles. This is possible because on the one hand the Riemann solver does not introduce values of w which are not present in the initial data (so that we can say that vehicles keep their initial value of w), and on the other hand each value of w corresponds to a different maximal density: Taking $p(\rho) = \rho^4$, we have $\max_v\{\rho(v, \bar{w})\} = \bar{w}^{\frac{1}{4}}$. Then the average "size" of vehicles associated to $w = \bar{w}$ is $\bar{w}^{-\frac{1}{4}}$. Low values of w characterize long vehicles (as their maximal density on the road is low), with low maximal velocity, whereas high values of w characterize small vehicles with large maximal velocity.

In [26], the authors consider traffic in presence of a slow moving vehicle, which reduces the road capacity, and assume that the effective capacity loss depends on the trace of w at the slow vehicle's location (local moving constraint). Here we introduce an example of non-local constraint depending on the total weight of the upstream vehicles.

Assuming that a first evaluation of the weight of a vehicle is its volume, we can estimate the total weight of vehicles present on a road section $[a, b] \subset \mathbb{R}$ by using the following formula:

$$m(t) = \int_a^b \rho\, w^{-\frac{3}{4}}\, \mathrm{d}x. \tag{21}$$

In this example we imagine to monitor the stretch of road upstream a bridge of limited carrying capacity. The entrance of the bridge is located at b. Starting from equation (21), we can consider a non-local constraint function of the following form

$$Q(t) = \begin{cases} q_{\lim}, & \text{if } \xi(t) \geqslant \bar{\xi}, \\ +\infty, & \text{otherwise,} \end{cases} \qquad \xi(t) = \frac{\int_a^b \rho\, w^{-\frac{3}{4}}\, \varphi(x)\, \mathrm{d}x}{\int_a^b \varphi(x)\, \mathrm{d}x}, \tag{22}$$

where φ is a weight function so that vehicles closer to b have a larger impact on the constraint activation.

In the next numerical example, in addition to consider as usual $p(\rho) = \rho^4$, we fix $a = -0.5$, $b = 0$, $\varphi(x) = 1$, $q_{\lim} = 0.195$, $\bar{\xi} = 0.7$ and set the initial data as

$$\bar{\rho}(x) = \begin{cases} 1.21, & \text{if } x \in [-1.5, -1.0], \\ 0.60, & \text{if } x \in [-1.0, -0.5], \\ 1.03, & \text{if } x \in [-0.5, 0.0], \\ 0.0, & \text{otherwise}, \end{cases} \qquad \bar{w}(x) = \begin{cases} 2.5, & \text{if } x < -1.0, \\ 0.5, & \text{if } x \in [-1.0, -0.5], \\ 1.5, & \text{if } x \in [-0.5, 0.0], \\ 0.0, & \text{if } x > 0. \end{cases}$$

We stress that the value of w on $x > 0$ is set arbitrarily in this example and does not modify the solution. The values of the densities are chosen so that the blocks have similar initial velocities.

The results are presented in Figure 14. The constraint activates immediately as a block of very high density, low-w vehicles approaches the bridge. It remains active as the block of less dense but larger vehicles is detected. The larger vehicles are much slower than the small ones when subject to the constraint, which explains the opening of vacuum on the bridge when they reach $x = 0$. The constraint being non-local, it ceases to act when the "potential incoming weight" is back to safe values. According to the numerical results, this happens at $t \approx 3.984$, time at which we can observe the creation of a rarefaction wave starting at $x = 0$, which indicates the increase in the through flow.

(A) Density (B) Density zoom (C) Flux zoom

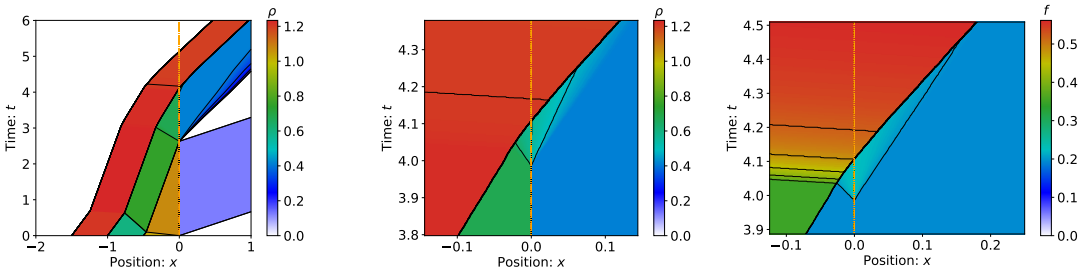

FIGURE 14. The numerical solution is here computed when the constraint on the flux Q is given by the non-local expression provided in equation (22). Thus, the constraint on the flux is a decreasing function of the total vehicle weight on a local upstream area of the constraint, namely on $[-0.5, 0.0]$. In this setting, the constraint on the flux remains activated until $t = 3.984$. Figure 14a represents the heat map of the density in space and time. Figures 14b and 14c represent the heat map of the density and of the flux, respectively, in space and time zoomed around the constraint location when the constraint deactivates.

6. CONCLUSIONS

In this paper we show that the second order ARZ model subject to local or non-local point constraints, as it was introduced in [4], can reproduce qualitative features that are characteristic of vehicular macroscopic phenomena at bottlenecks (capacity drop, Faster is Slower, phantom jams). These effects are shown to be persistent for large intervals of values of parameters.

We designed and implemented an adapted version of the Glimm scheme, featuring a non-classical Riemann solver at the constraint locations, and we show its numerical convergence. The results presented in this paper allow us to consider more complex models for traffic in presence of constraints and moving obstacles, traffic models on tree shaped networks and management problems in the same spirit of [14, 16].

Acknowledgment

The work of C. Donadello, U. Razafison and J. Y. Rolland is partially supported by the EIPHI Graduate School (contract ANR-17-EURE-0002) and the Région Bourgogne-Franche-Comté. C. Donadello, U. Razafison and B. Polizzi also acknowlegde the financial support of the International Emerging Action CNRS *Conpanhye*. M.D. Rosini acknowledges financial support from the PRIN 2022 project *Modeling, Control and Games through Partial Differential Equations* (D53D23005620006), funded by the European Union - Next Generation EU; the INdAM - GNAMPA Research Project *Modeling and Analysis through Conservation Laws*, code CUP E53C23001670001. The work of B. Polizzi have been partially supported by the Université Côte d'Azur, Inria, France.

References

[1] Boris Andreianov, Carlotta Donadello, Ulrich Razafison, and Massimiliano D. Rosini. Riemann problems with non–local point constraints and capacity drop. *Mathematical Biosciences and Engineering*, 12(2):259–278, 2015.

[2] Boris Andreianov, Carlotta Donadello, Ulrich Razafison, and Massimiliano D. Rosini. Qualitative behaviour and numerical approximation of solutions to conservation laws with non-local point constraints on the flux and modeling of crowd dynamics at the bottlenecks. *ESAIM: M2AN*, 50(5):1269–1287, 2016.

[3] Boris Andreianov, Carlotta Donadello, and Massimiliano D. Rosini. Crowd dynamics and conservation laws with nonlocal constraints and capacity drop. *Mathematical Models and Methods in Applied Sciences*, 24(13):2685–2722, 2014.

[4] Boris Andreianov, Carlotta Donadello, and Massimiliano D. Rosini. A second-order model for vehicular traffics with local point constraints on the flow. *Mathematical Models and Methods in Applied Sciences*, 26(04):751–802, 2016.

[5] Boris Andreianov, Paola Goatin, and Nicolas Seguin. Finite volume schemes for locally constrained conservation laws. *Numerische Mathematik*, 115:609–645, 2010.

[6] Boris P. Andreianov, Carlotta Donadello, Ulrich Razafison, Julien Yves Rolland, and Massimiliano D. Rosini. Solutions of the Aw-Rascle-Zhang system with point constraints. *Networks and Heterogeneous Media*, 11(1):29–47, 2016.

[7] Abdellahi Aw and Michel Rascle. Resurrection of "second order" models of traffic flow. *SIAM J. Appl. Math.*, 60(3):916–938 (electronic), 2000.

[8] Florent Berthelin and Damien Broizat. A model for the evolution of traffic jams in multi-lane. *Kinet. Relat. Models*, 5(4):697–728, 2012.

[9] Florent Berthelin, Pierre Degond, Marcello Delitala, and Michel Rascle. A model for the formation and evolution of traffic jams. *Archive for Rational Mechanics and Analysis*, 187(2):185–220, Feb 2008.

[10] Florent Berthelin, Thierry Goudon, Bastien Polizzi, and Magali Ribot. Asymptotic problems and numerical schemes for traffic flows with unilateral constraints describing the formation of jams. *Networks and Heterogeneous Media*, 12(4):591–617, 2017.

[11] Christophe Chalons and Paola Goatin. Transport-equilibrium schemes for computing contact discontinuities in traffic flow modeling. *Commun. Math. Sci.*, 5(3):533–551, 09 2007.

[12] Christophe Chalons, Paola Goatin, and Nicolas Seguin. General constrained conservation laws. Application to pedestrian flow modeling. *Netw. Heterog. Media*, 8(2):433–463, 2013.

[13] Phillip Colella. Glimm's method for gas dynamics. *SIAM J. Sci. Statist. Comput.*, 3(1):76–110, 1982.

[14] Rinaldo M. Colombo, Giancarlo Facchi, Giulio Maternini, and Massimiliano D. Rosini. On the continuum modeling of crowds. In *Hyperbolic problems: theory, numerics and applications*, volume 67 of *Proc. Sympos. Appl. Math.*, pages 517–526. Amer. Math. Soc., Providence, RI, 2009.

[15] Rinaldo M. Colombo and Paola Goatin. A well posed conservation law with a variable unilateral constraint. *J. Differential Equations*, 234(2):654–675, 2007.

[16] Rinaldo M. Colombo, Paola Goatin, and Massimiliano D. Rosini. On the modelling and management of traffic. *ESAIM: Mathematical Modelling and Numerical Analysis*, 45(5):853–872, 2011.

[17] Pierre Degond and Marcello Delitala. Modelling and simulation of vehicular traffic jam formation. *Kinet. Relat. Models*, 1(2):279–293, 2008.

[18] Maria Laura Delle Monache and Paola Goatin. A front tracking method for a strongly coupled PDE-ODE system with moving density constraints in traffic flow. *Discrete and Continuous Dynamical Systems - Series S*, 7(3):435–447, June 2014.

[19] Maria Laura Delle Monache and Paola Goatin. Scalar conservation laws with moving constraints arising in traffic flow modeling: an existence result. *Journal of Differential equations*, 257(11):4015–4029, 2014.

[20] Carlos Gershenson and Dirk Helbing. When slower is faster. *Complexity*, 21(2):9–15, 2015.
[21] Marte Godvik and Harald Hanche-Olsen. Existence of solutions for the Aw–Rascle traffic flow model with vacuum. *Journal of Hyperbolic Differential Equations*, 05, 11 2011.
[22] Eric J. Gonzales and Eleni Christofa. Empirical assessment of bottleneck congestion with a constant and peak toll: San Francisco–Oakland Bay Bridge. *EURO Journal on Transportation and Logistics*, 3(3):267–288, 2014.
[23] Dirk Helbing, Illes Farkas, and Tamas Vicsek. Simulating dynamical features of escape panic. *Nature*, 407(6803):487–490, 2000.
[24] Cheolsun Kim, Dong-Kyu Kim, Seung-Young Kho, Seungmo Kang, and Koohong Chung. Dynamically determining the toll plaza capacity by monitoring approaching traffic conditions in real-time. *Applied Sciences*, 6(3):87, 2016.
[25] Stanislav N. Kružhkov. First order quasilinear equations with several independent variables. *Mat. Sb. (N.S.)*, 81 (123):228–255, 1970.
[26] Thibaul Liard, Francesca Marcellini, and Benedetto Piccoli. The Riemann problem for the GARZ model with a moving constraint. In *Hyperbolic Problems: Theory, Numerics, Applications*, pages 524 – 530, 2018.
[27] M. James Lighthill and Gerald B. Whitham. On Kinematic Waves. II. A Theory of Traffic Flow on Long Crowded Roads. *Royal Society of London Proceedings Series A*, 229:317–345, May 1955.
[28] Jie Lin and Dan Yu. Traffic-related air quality assessment for open road tolling highway facility. *Journal of Environmental Management*, 88(4):962 – 969, 2008.
[29] Yun-Guang Lu. Existence of global bounded weak solutions to nonsymmetric systems of Keyfitz–Kranzer type. *Journal of Functional Analysis*, 261(10):2797–2815, 2011.
[30] Daniel R. Parisi and Claudio O. Dorso. Microscopic dynamics of pedestrian evacuation. *Physica A: Statistical Mechanics and its Applications*, 354(0):606 – 618, 2005.
[31] Paul I. Richards. Shock waves on the highway. *Operations Research*, 4(1):42–51, 1956.
[32] Anupam Srivastava and Nikolas Geroliminis. Empirical observations of capacity drop in freeway merges with ramp control and integration in a first-order model. *Transportation Research Part C: Emerging Technologies*, 30:161–177, 2013.
[33] H. Eugene Stanley. Non-equilibrium physics: Freezing by heating. *Nature*, 404(6779):718–719, 2000.
[34] Yuki Sugiyama, Minoru Fukui, Macoto Kikuchi, Katsuya Hasebe, Akihiro Nakayama, Katsuhiro Nishinari, Shin ichi Tadaki, and Satoshi Yukawa. Traffic jams without bottlenecks–experimental evidence for the physical mechanism of the formation of a jam. *New Journal of Physics*, 10(3):033001, 2008.
[35] Abraham Sylla. A LWR model with constraints at moving interfaces. *ESAIM: M2AN*, 56(3):1081–1114, 2022.
[36] Eleuterio F. Toro. *Riemann solvers and numerical methods for fluid dynamics*. Springer-Verlag, Berlin, 1997. A practical introduction.
[37] H. Michael Zhang. A non-equilibrium traffic model devoid of gas-like behavior. *Transportation Research Part B: Methodological*, 36(3):275 – 290, 2002.

Appendices

Appendix A. Well-posedness for the ADR model

In this section we recall the existence result obtained in [4] for the ADR model (1). The choice of using the Riemann invariants (v, w) as independent variables is very convenient in the theoretical study of the ARZ system, in particular for the description of the Riemann solver and the definition of entropy pairs, the latter being multi-valued in conservative variables. Also, the total variation of solutions of the ARZ model written in Riemann invariants does not increase in time, while it generally does when we use the conservative variables (ρ, y). This is a fundamental ingredient toward the global existence results in [21] and [29].

Following the same approach, in [4] the authors obtained a priori bounds on the total variation of the solution for the ADR model in the (v, w) variables, and defined suitable entropy pairs. In this section we give a short account of their results. We stick to their notations to facilitate the reader who may want to go deeper into the details of [4]. However, we stress that in the next sections the outputs of our numerical simulations are expressed in the variables ρ and v, as these quantities (mean density and velocity), together with their product $q = \rho\, v$ (density flux), are easier to compare to experimental data.

The definition of entropy solution for the constrained Cauchy problem (1) with a given piece-wise constant in time constraint function Q is introduced in [6, Definition 4.2], see also [4, Definition 3.3]. Such definition is obtained by adding a term that accounts for the constraint in the classical definition of entropy solution given by Kruzhkov in [25], in analogy to what is done for the scalar case in [5, 12, 15] and, for non-local constraints, in [3, Definition 2.1].

Definition A.1. *Let $(\bar v, \bar w) \in \mathbf{BV}(\mathbb{R}; \mathcal{W})$ and $Q \in \mathbf{PC}(\mathbb{R}_+; \mathbb{R}_+)$. We say that (v, w) is an entropy solution to (1) if it is in $\mathbf{L}^\infty\big(\mathbb{R}_+; \mathbf{BV}(\mathbb{R}; \mathcal{W})\big) \cap C^0\big(\mathbb{R}_+; \mathbf{L}^1_{\rm loc}(\mathbb{R}; \mathcal{W})\big)$ and*

(1) it satisfies the initial condition $(v, w)(0, x) = (\bar v, \bar w)(x)$ for a.e. x in $\mathbb{R}$;
(2) it satisfies the constraint condition $[v\, \rho(v, w)](t, 0^\pm) \leqslant Q(t)$ for a.e. t in $\mathbb{R}_+$;
(3) for any test function $\phi \in C^\infty_c(\mathbb{R}_+ \times \mathbb{R}; \mathbb{R})$ it satisfies

$$\iint_{\mathbb{R}_+\times\mathbb{R}} \rho(v, w)\, [\phi_t + v\, \phi_x] \begin{pmatrix} v \\ w \end{pmatrix} \mathrm{d}x\, \mathrm{d}t = \begin{pmatrix} 0 \\ 0 \end{pmatrix};$$

(4) for any non-negative test function $\phi \in C^\infty_c(\mathbb{R}_+ \times \mathbb{R}; \mathbb{R})$ and $k \in \mathbb{R}_+$ it satisfies

$$\iint_{\mathbb{R}_+\times\mathbb{R}} [\mathcal{E}_k(v, w)\, \phi_t + \mathcal{Q}_k(v, w)\, \phi_x]\ \mathrm{d}x\, \mathrm{d}t + \int_{\mathbb{R}_+} \mathcal{N}_k(v, w, Q)\, \phi(t, 0)\ \mathrm{d}t \geqslant 0,$$

where

$$\mathcal{E}_k(v, w) = \begin{cases} 0 & \text{if } v \leqslant k, \\ 1 - \dfrac{\rho(v, w)}{\rho(k, w)} & \text{if } v > k, \end{cases} \qquad \mathcal{Q}_k(v, w) = \begin{cases} 0 & \text{if } v \leqslant k, \\ k - \dfrac{v\, \rho(v, w)}{\rho(k, w)} & \text{if } v > k, \end{cases}$$

$$\mathcal{N}_k(v, w, Q) = \begin{cases} [v\, \rho(v, w)](t, 0) \left[\dfrac{k}{Q(t)} - \dfrac{1}{p^{-1}([w(t, 0) - k]^+)}\right]^+, & \text{if } Q(t) \neq 0, \\ k, & \text{otherwise.} \end{cases}$$

The theorem on existence of entropy solutions to the constrained Cauchy problem (1) in [4] needs some assumptions on p, $(\bar v, \bar w)$ and Q, which we introduce now.

Assumptions on the initial data $(\bar v, \bar w)$: For every $x \in \mathbb{R}$, the left and the right limit values of the initial data at x belong to a domain $\mathfrak{G} \subset \mathcal{W}$, namely

$$(\bar W) \qquad \begin{pmatrix} (\bar v, \bar w)(x^-) \\ (\bar v, \bar w)(x^+) \end{pmatrix} \in \mathfrak{G} = \left\{ \begin{pmatrix} W_\ell \\ W_r \end{pmatrix} \in \mathcal{W}^2 \colon \begin{array}{l} W_\ell \in \mathcal{W}_0 \\ W_r \in \mathcal{W}_0 \end{array} \right\} \Rightarrow W_\ell = W_r, \\ \left. \begin{array}{l} W_\ell \in \mathcal{W}_0^c \\ W_r \in \mathcal{W}_0 \end{array} \right\} \Rightarrow W_r = (w_\ell, w_\ell) \Bigg\}.$$

Remark A.1. *The assumption $\bar W$ is important for the theoretical analysis of system* (1)*, because a crucial ingredient in the proof of existence is the uniform bound on the total variation of the w component of the solution. In the implementation of our numerical scheme we need to consider initial data in the whole $\mathcal{W}^2$. We refer to Section 2 for more details.*

Assumptions on the initial datum $\bar w$ and the constraint function Q: The most delicate estimates in [4] deal with the possible increase of the total variation associated to the interaction of waves at the constraint location and the changes in the value of the constraint. To keep track of them the authors introduce the functional

$$J(Q, w) = \check v(Q, w) - \hat v(Q, w) \in \mathbb{R}_+$$

for $\check v(Q, w)$ and $\hat v(Q, w)$ defined in (7). In order to achieve the well-posedness of the constrained Cauchy problem we need to enforce the following condition on Q and $\bar w$

$$(\mathrm{Q}) \qquad \sum_{\substack{t>0 \text{ s.t.} \\ Q(t-) \neq Q(t+)}} \left[\sup_{y \in \mathbb{R}_-} \Big| \mathrm{TV}\big(J\left(Q(t-), \bar w\right); (-\infty, y]\big) - \mathrm{TV}\big(J\left(Q(t+), \bar w\right); (-\infty, y]\big) \Big| \right],$$

is bounded and $\mathbb{R}_- \ni x \mapsto J(Q(0), \bar w(x)) \in \mathbb{R}_+$ has bounded total variation.

Theorem A.1 (Theorem 3.1 in [4])**.** *Assume* (3)*. Let $(\bar v, \bar w) \in \mathbf{BV}(\mathbb{R}; \mathcal{W})$ satisfy $(\bar W)$, and $Q \colon \overline{\mathbb{R}}_+ \to \mathbb{R}_+$ be piecewise constant and satisfying* (Q)*. Then the Cauchy problem* (1) *with initial datum $(\bar v, \bar w)$ and constraint Q admits a constrained entropy solution $(v, w) \in C^0\left(\mathbb{R}_+; \mathbf{BV}\left(\mathbb{R}; \mathcal{W}\right)\right)$ in the sense of Definition A.1. Furthermore, there exist two constants C and L such that for any $t, s \in \mathbb{R}_+$*

$$\mathrm{TV}\big((v, w)(t)\big) \leqslant C, \quad \|(v, w)(t) - (v, w)(s)\|_{\mathbf{L}^1} \leqslant L\,|t - s|, \quad \|(v, w)(t)\|_{\mathbf{L}^\infty} \leqslant \|\bar w\|_{\mathbf{L}^\infty} = V_0.$$

Appendix B. Non-local constraint depending on the upstream density (piece-wise constant)

In this example, we consider a constraint whose value depends on the averaged mean of the density component of the solution in an upstream neighborhood of the constraint location

$$(23) \qquad Q(t) = \begin{cases} q_0, & \text{if } \xi(t) \leqslant \bar\xi, \\ q_1, & \text{otherwise,} \end{cases} \qquad \text{where } \xi(t) = \frac{\int_\Omega \rho(t, x)\varphi(x)\,\mathrm{d}x}{\int_\Omega \varphi(x)\,\mathrm{d}x}.$$

This kind of constraint has been considered in [3], in association with the LWR first-order model, to model the capacity drop effect. See also [2] for the theoretical and numerical analysis of first-order models featuring more general non-local constraints. In the simulation below the constraint is located at $x = 0$ and we fix the numerical values of its parameters as $q_0 = 0.7$, $q_1 = 0.4$, $\bar\xi = 1$, $\Omega = [-1, 0]$ and $\varphi(x) = 2x + 2$. The initial condition consists of a single block of constant density and velocity

$$(24) \qquad \big(\bar\rho(x), \bar v(x)\big) = \begin{cases} (1, 1), & \text{if } x \in [-3.5, -1.5], \\ (0, 0), & \text{otherwise.} \end{cases}$$

The evolution of the enforced constraint value over time is represented in Figure 15b. Figure 15a represents the heat map of the density in space and time. As in Section 4.2, there is only one block with constant density and velocity in the initial data, therefore the Lagrangian marker is

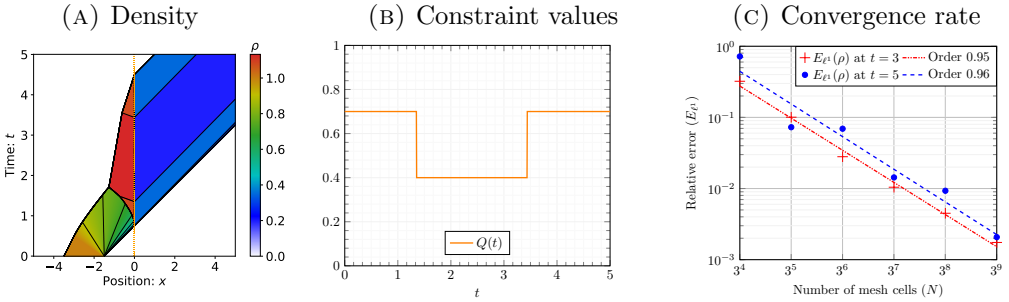

FIGURE 15. The numerical solution is here computed when the initial data is as in (24) and the constraint on the flux Q is the non-local functional provided in equation (23). The constraint Q is a discontinuous decreasing function of the weighted averaged density in the local upstream area of the constraint, namely on $[-1, 0]$. The constraint value over time is represented in Figure 15b. Figure 15a represents the heat map of the density in space and time. Figure 15c represents the convergence rate toward the reference solution computed using the numerical scheme proposed in [1] for two different times.

constant and takes the value $w = 2$. The model reduces to the constraint LWR model, see [1], with density flux $f(\rho) = \rho\,(2 - \rho^4)$. Thus, here also the reference solution used to assess the convergence of the scheme is computed using the method presented in this paper which is based on Godunov numerical scheme and whose convergence has been theoretically proved. As shown in Figure 15c the convergence rate is 0.95 at $t = 3$ when the constraint is at its lower level, and 0.96 at the final time when the constraint has returned to its higher level.

(Carlotta Donadello) UNIVERSITÉ MARIE ET LOUIS PASTEUR, CNRS, LMB (UMR 6623), F-25000 BESANÇON, FRANCE.
Email address: carlotta.donadello@univ-fcomte.fr

(Bastien Polizzi) UNIVERSITÉ MARIE ET LOUIS PASTEUR, CNRS, LMB (UMR 6623), F-25000 BESANÇON, FRANCE.
Email address: bastien.polizzi@univ-fcomte.fr

(Ulrich Razafison) UNIVERSITÉ MARIE ET LOUIS PASTEUR, CNRS, LMB (UMR 6623), F-25000 BESANÇON, FRANCE.
Email address: ulrich.razafison@univ-fcomte.fr

(Julien Yves Rolland) UNIVERSITÉ MARIE ET LOUIS PASTEUR, CNRS, LMB (UMR 6623), F-25000 BESANÇON, FRANCE.
Email address: julien.rolland@univ-fcomte.fr

(Massimiliano D. Rosini) INSTYTUT MATEMATYKI, UNIWERSYTET MARII CURIE-SKŁODOWSKIEJ,, PLAC MARII CURIE-SKŁODOWSKIEJ 1, 20-031 LUBLIN, POLAND, AND DIPARTIMENTO DI ECONOMIA AZIENDALE, UNIVERSITÀ DEGLI STUDI "GABRIELE D'ANNUNZIO",, VIALE PINDARO 42, 65127 PESCARA, ITALY
Email address: mrosini@umcs.lublin.pl